Static Softening in a Ni-30Fe Austenitic Model Alloy After Hot Deformation: Microstructure and Texture Evolution

HOSSEIN BELADI, PAVEL CIZEK, ADAM S. TAYLOR, GREGORY S. ROHRER, and PETER D. HODGSON

In the current study, the microstructure and texture characteristics of a model Ni-30Fe austenitic alloy were investigated during hot deformation and subsequent isothermal holding. The deformation led to the formation of self-screening arrays of microbands within a majority of grains. The microbands characteristics underwent rather modest changes during the post-deformation annealing, which suggests that limited dislocation annihilation occurs within the corresponding dislocation walls. The fraction of statically recrystallized (SRX) grains progressively increased with the holding time and closely matched the softening fraction measured from the offset flow stress approach. The corresponding texture was weak and preserved its character with the holding time. There was no pronounced temperature effect on the grain boundary character distribution after the completion of SRX. The Σ3 and Σ9 coincidence site lattice boundaries were characterized as (111) pure twist and (1−14) symmetric tilt types, respectively. Nonetheless, the recrystallization temperature slightly affected the grain boundary network.

I. INTRODUCTION

STATIC recrystallization (SRX) is one of the most common and important restoration mechanisms taking place during thermomechanical processing of steels.[1] This process involves the nucleation and growth of dislocation-free grains in the deformed matrix, which simultaneously undergoes recovery/dislocation annihilation, during the post-deformation annealing. SRX has attracted a significant attention among different research groups around the world, largely focusing on the mechanical response, kinetics, and grain size changes as a function of thermomechanical parameters *e.g.* References 2 through 4. However, for the case of steels in the austenite state, there is currently a limited understanding of the evolution of the dislocation substructure characteristics of the deformed (statically recovered) matrix, which coexists with recrystallized grains and is progressively consumed during SRX process. In addition, more information is required regarding the crystallographic texture evolution for both the deformed austenite matrix and SRX grains during the post-deformation annealing. This is largely for the reason that the phase transformation occurring

in steels on cooling prevents the direct investigation of the austenite microstructure and texture behavior during deformation and post-deformation annealing process. This has led to the design of model austenitic alloys (*e.g.*, Ni-30Fe alloy), which do not transform on cooling and have similar stacking fault energy to low-carbon low-alloy steels in the high-temperature austenite regime.[5–8] The latter ensures similar deformation behavior to the steel at high deformation temperatures while the former enables us to study the hot deformed austenite microstructure at ambient temperature.

The austenitic model alloys have been widely used to study the deformed microstructure obtained under different thermomechanical processing conditions, *e.g.* References 6 through 14. These studies have revealed that the deformation of austenite, in the hot working temperature range employed for steel, largely leads to the formation of arrays of extended parallel planar dislocation walls bounding so called "microbands" (MBs) within a majority of grain interiors. These MB arrays are typically characterized by systematically alternating misorientations across consecutive extended boundaries.[12–17] It is of interest to elucidate how such unique self-screening dislocation arrangements impact on the dislocation annihilation processes during the post-deformation annealing.

It has been demonstrated that the MB characteristics (*i.e.*, misorientation and boundary spacing), which govern the deformation stored energy within hot deformed austenite, are significantly influenced by the austenite grain orientation.[12,13,17] However, it is not clear how the orientation dependence of the substructure characteristics influences the restoration processes

HOSSEIN BELADI, PAVEL CIZEK, ADAM S. TAYLOR, and PETER D. HODGSON are with the Institute for Frontier Materials, Deakin University, Geelong, VIC 3216, Australia. Contact e-mail: hossein.beladi@deakin.edu.au GREGORY S. ROHRER is with the Department of Materials Science and Engineering, Carnegie Mellon University, Pittsburgh, PA 15213-3890.
Manuscript submitted May 30, 2016.
Article published online November 29, 2016.

(*i.e.*, recovery/dislocation annihilation and recrystallization) taking place during the post-deformation annealing. Indeed, the variation in the initial stored energy between differently oriented grains may potentially lead to differences in the rate of deformed matrix consumption by the dislocation-free SRX grains during the recrystallization process. This may affect the crystallographic texture of the remaining unrecrystallized matrix and, consequently, also the overall texture of partially recrystallized material.

In addition, SRX is one of the main routes to manipulate the grain boundary network in metals.[18] The extent of the coincident site lattice (CSL) boundaries development, which may contribute to the characteristics of the final phase transformed product in steels, is significantly influenced by the thermomechanical processing parameters (*i.e.*, strain and deformation temperature).[18] Among different thermomechanical parameters, the deformation temperature has to date received limited attention, though it is known to alter the stacking fault energy of austenite,[19] potentially resulting in different CSL boundaries development.

The aim of the current work was to investigate the deformed state characteristics, as well as the post-deformation static softening processes, in a model Ni-30Fe austenitic alloy deformed under similar conditions to those used in the hot working of low-carbon steels. The investigation used interrupted hot torsion tests comprising two deformation passes separated by varied isothermal holding. The second pass was used to determine how much softening occurred during the holding. A parallel set of samples were water quenched after the holding step, so that the microstructure could be evaluated. Electron back-scattered diffraction (EBSD) in conjunction with transmission electron microscopy (TEM) was used to study the hot deformation microstructure and texture characteristics along with the evolution of grain structure, dislocation substructure, and crystallographic texture during post-deformation annealing. The EBSD technique also facilitated the measurement of the grain boundary character distribution for two SRX grain structures, obtained at different temperatures, using the five-parameter crystallographic approach.[20]

II. EXPERIMENTAL METHODS

An austenitic model alloy with a composition of Ni-29.5Fe-0.01C-0.02Mn (in wt pct) was used in the current study. As already mentioned above, this alloy is well suited for modeling of the microstructure evolution during hot deformation of low-carbon steels.[5–8,21] A hot torsion deformation simulator, described elsewhere,[22] was used to deform the samples. The specimens had a gauge length of 20 mm and a gauge diameter of 6.7 mm. Von Mises equivalent stress-strain values were derived from the torque-twist data using the method based on the analysis by Fields and Backofen.[23]

The specimens were reheated to 1473 K (1200 °C), held for 80 seconds and then subjected to two roughing

deformation steps using equal strains of 0.4 and performed at a strain rate of 1 s^{-1}. Each deformation step was followed by holding for 40 seconds during which the microstructure became fully recrystallized (Figure 1). This led to a homogeneous grain distribution with an average grain size of about 49 μm. The specimens were subsequently cooled (2 K/s) to 1273 K (1000 °C), and held for 120 seconds. Afterwards, interrupted torsion tests (*i.e.*, double hit deformation) were carried out to study the kinetics of post-deformation softening. Each experiment involved deforming at 1273 K (1000 °C) to a strain of 0.3 (*i.e.*, the first deformation) at a strain rate of 1 s^{-1}, followed by holding for a given time and then re-deforming to a strain of 0.2 (*i.e.*, the second deformation, Figure 1). The softening fraction, SF, at a given thermomechanical condition was estimated as

$$SF = ((\sigma3 - \sigma2)/(\sigma3 - \sigma1)) \times 100 \, [\text{pct}], \quad [1]$$

where σ_1 is the yield stress of the first deformation; σ_2 is the yield stress of the second deformation, and σ_3 is the flow stress at the end of first deformation. Some samples deformed to a strain of 0.3 were water quenched either immediately after deformation or at a given post-deformation holding time to examine the microstructure/texture development during post-deformation softening.

Microstructural characterization was performed on tangential sections at a depth of ~100 μm below the surface of the gauge length using EBSD and TEM techniques. Samples for EBSD were prepared by standard mechanical polishing finished with a colloidal silica slurry polish. EBSD study was carried out using the Zeiss LEO 1530 FEG SEM and FEI Quanta 3D FEG SEM/FIB instruments both operated at 20 kV. The former instrument was equipped with the fully automatic HKL Technology EBSD attachment (*i.e.*, the HKL Channel 5 software), mainly used for characterization of substructure and crystallographic texture. The latter employed the TexSEM Laboratories (TSL) EBSD hardware and software for data acquisition and
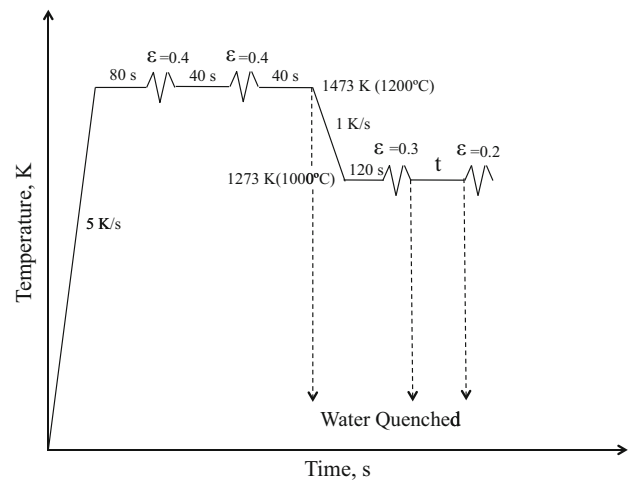

Fig. 1—Schematic representation of thermomechanical processing routes. t represents the post-deformation holding time, varying from 0 to 150 s.
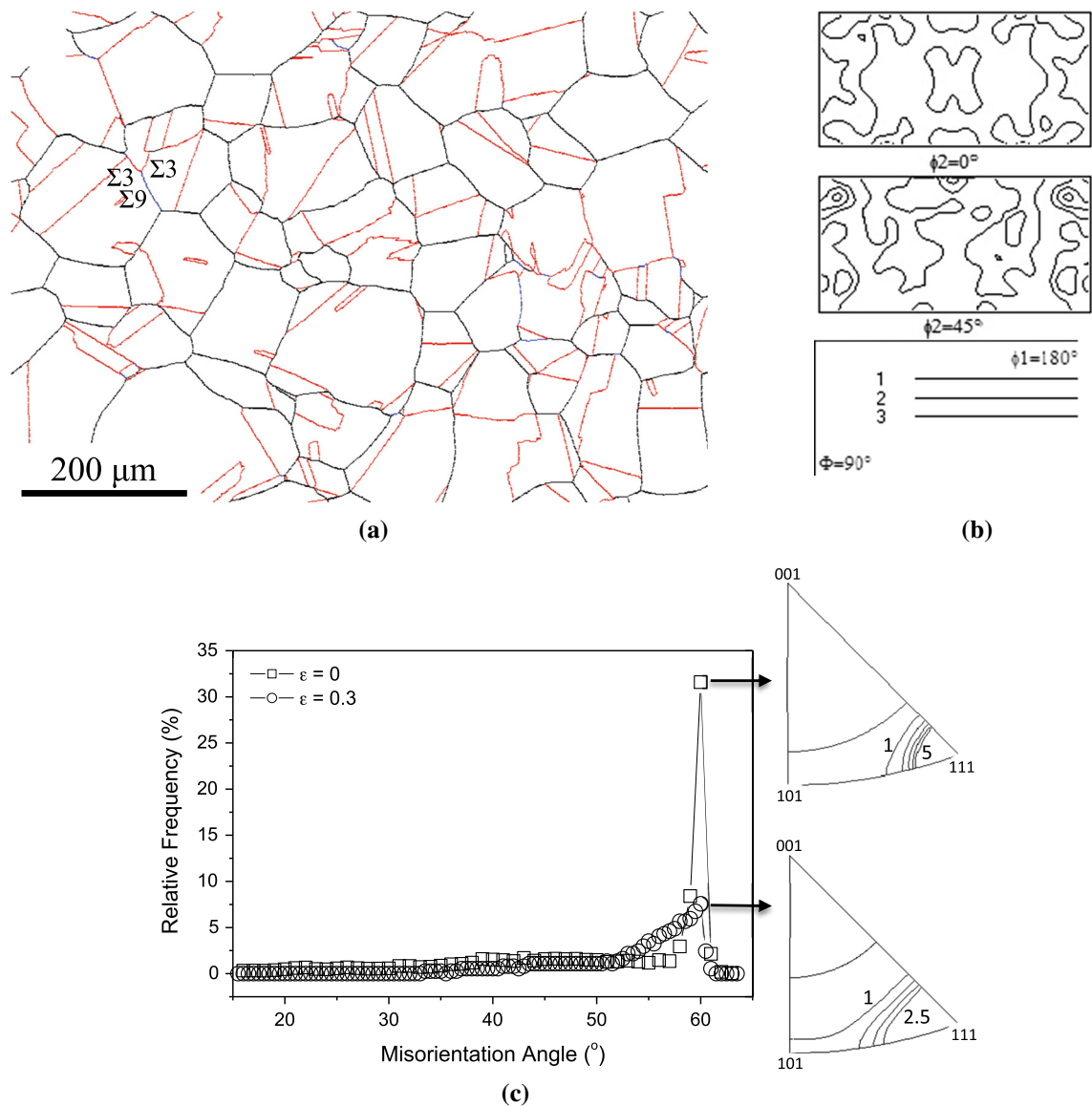
(a)

(b)

(c)

Fig. 2—Microstructure (*a*) and ODF texture (*b*) of SRX grains formed at 1473 K (1200 °C). The black, red, and blue lines represent grain boundaries with misorientations above 15 deg, Σ3, and Σ9 boundaries, respectively. (*c*) Misorientation angle distribution of grain boundaries at different conditions, SRX at 1473 K (1200 °C, starting microstructure) and deformed at a strain of 0.3 at 1273 K (1000 °C), together with the corresponding misorientation axis vectors in the crystal lattice coordinates. The numbers on the standard stereographic triangles represent the contour intensity in multiples of a random distribution (Color figure online).

post-processing to characterize the distribution of grain boundary planes.

EBSD maps were acquired using a step size of 0.1 μm and 3 μm for characterization of the grain substructure and the crystallographic texture, respectively. Pattern solving efficiencies generally varied between 95 and 98 pct depending upon the step size and deformation condition of a given sample. An area of about 10 × 1 mm^2 was scanned at each thermomechanical processing condition (*i.e.*, holding time) to investigate the evolution of crystallographic texture of both the statically recrystallized and deformed (recovered) matrix grains during hot deformation. The EBSD maps were initially cleaned using the Kuwahara filtering routine to enhance the sub-boundaries and reduce the orientation

noise. SRX grains were then separated from the deformed matrix using the subsetting routine in the Channel 5 software, based on the internal average misorientation angle within a grain. If the average misorientation angle did not exceed 0.2 deg, the grain was considered recrystallized. This facilitated the determination of the SRX fraction. The mean SRX grain size was determined as an average of the mean linear intercepts measured in the horizontal and vertical directions. The crystallographic texture was described using the orientation distribution function (ODF),[24] calculated from the EBSD data adopting the monoclinic symmetry of the torsion specimens. Each texture component was specified by its Euler angles, with 15 deg deviation from the ideal orientation, and presented as a

given color in the EBSD orientation maps using the Channel 5 software.

In order to characterize the distribution of grain boundary planes, multiple EBSD maps were acquired using a step size of 1 μm on a hexagonal grid using TSL software for the fully recrystallized structures at 1473 K and 1273 K (1200 °C and 1000 °C), covering a total area of approximately 1 × 12 mm^2. The average confidence index generally varied between 0.80 and 0.85. A grain dilation clean-up function in TSL software was employed for all the orientation maps to remove ambiguous data. A single orientation was then assigned to a given grain through averaging all orientation data belonging to that grain. Boundary line traces/segments were extracted after smoothing of uneven grain boundaries using the reconstruction grain boundary function in TSL software and employing a boundary deviation limit of 2 pixels (*i.e.,* 2 μm). There were more than 50,000 line traces after excluding the boundary segments of less than 3 μm. These line traces were employed to calculate the five-parameter grain boundary character distribution using an automated stereological approach described in detail elsewhere.[20] The analysis was implemented at 9 bins per 90 deg level of discretization, offering about 8.2 deg resolution (*i.e.*, 97 pct of the bins contained at least ten observations).
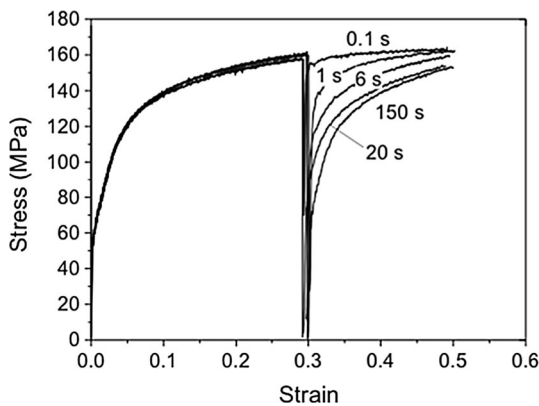

Fig. 3—Double-deformation flow curves obtained at a temperature of 1273 K (1000 °C) and a strain rate of 1 s^{-1} for different holding times.

To produce TEM foils, disks of 3 mm in diameter were taken from tangential sections at a depth of ~100 μm below the surface of the gauge length. Subsequently, they were mechanically ground to a thickness of about 70 μm and then twin-jet electropolished using a solution containing 5 pct perchloric acid and 95 pct methanol at a temperature of about 243 K (−30 °C) and a voltage of 20 V. TEM examination of the foils was performed using a JEM 2100F microscope operated at 200 kV.

III. RESULTS AND DISCUSSION

A. *Starting Recrystallized State*

The microstructure of the material subjected to two SRX cycles at 1473 K (1200 °C), taking place during two-pass roughing deformation with a strain of 0.4 in each pass followed by holding for 40 seconds, displayed an average grain size of ~49 μm (Figure 2(a)). The corresponding crystallographic texture was relatively weak, being characterized by a maximum of 3.1 times random (Figure 2(b)). There was a pronounced peak centered at about 60 deg in the misorientation histogram for the above SRX microstructure (Figure 2(c)). The misorientation axis vectors related to high-angle boundaries were strongly clustered around the ⟨111⟩ direction in the standard stereographic triangle (Figure 2(c)). This demonstrates that Σ3 first-order twin boundaries characterized by 60 deg/⟨111⟩ misorientation represented a significant volume fraction of the pre-existing high-angle boundaries.

B. *Hot Deformed State*

The stress-strain curve obtained at 1273 K (1000 °C) displayed a pronounced work hardening behavior (Figure 3). The flow curves of the first deformation (*i.e.*, ε = 0.3) for all holding times were very similar, indicating that the experiments were well duplicated. In other words, the specimens subjected to different interrupted torsion tests reflected the expected progress of softening with the incremented holding time after the first-pass deformation.

The initial coarse grains became elongated along the shear direction at a strain of 0.3 (Figure 4(a)). The

Table I. Ideal Torsion Texture Components in Austenite for φ_2 = 0 and 45 deg Sections[25]

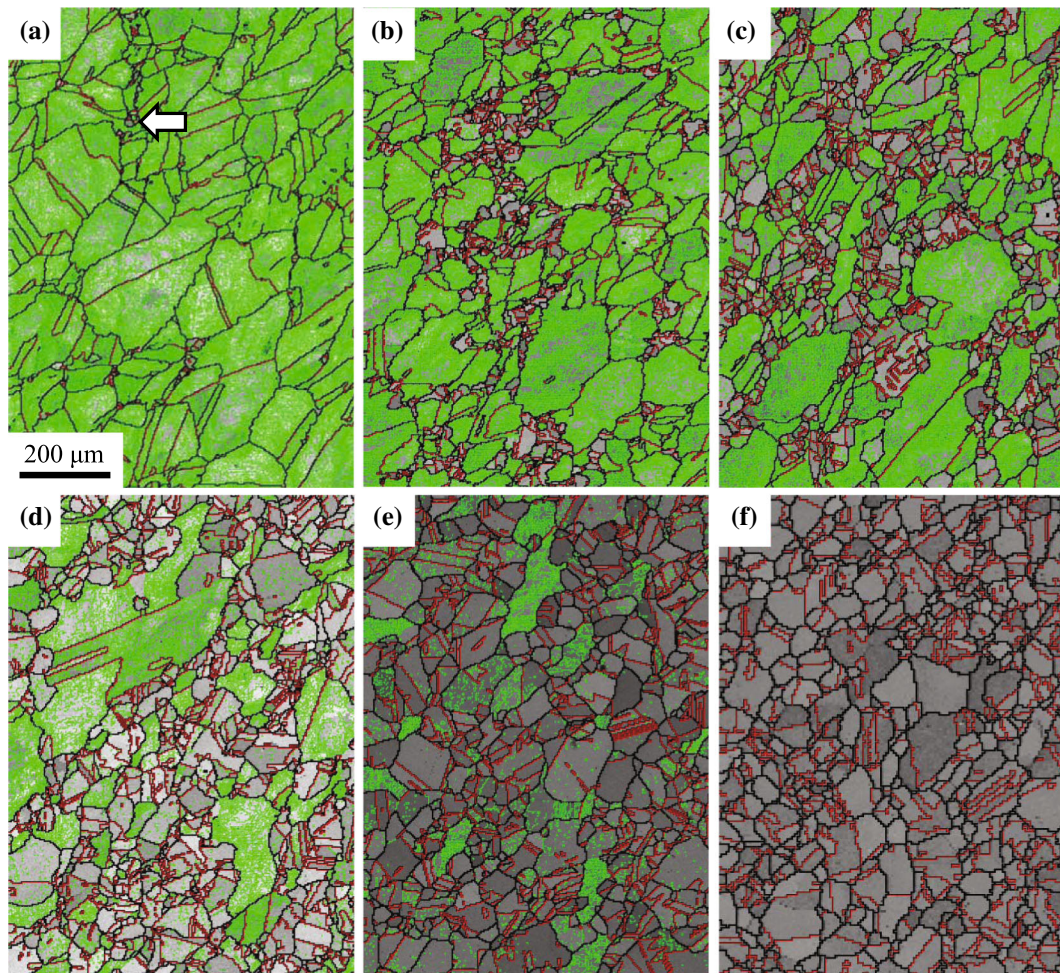| Orientation	(hkl)[uvw]	φ_1	Φ	φ_2
A1	(1−11)[110]	0.0	35.3	45.0
A2	(−11−1)[−1−10]	180.0	35.3	45.0
A1*	(111)[−1−12]	35.3	45.0	0.0/90.0
		125.3	90.0	45.0
A2*	(111)[11−2]	144.7	45.0	0.0/90.0
		54.7	90.0	45.0
B1	(1−12)[110]	0.0/120.0	54.7	45.0
B2	(−11−2)[−1−10]	60.0/180.0	54.7	45.0
C	{001}⟨110⟩	90.0	45.0	0.0/90.0
		0.0/180.0	90.0	45.0
R	(100)[011]	45	0.0	0.0

Fig. 4—EBSD maps obtained after deformation at 1273 K (1000 °C) with $\varepsilon = 0.3$ and holding for different post-deformation annealing times, followed by water-quenching: (*a*) 0 s, (*b*) 1 s, (*c*) 2 s, (*d*) 6 s, (*e*) 20 s, and (*f*) 150 s. The green regions represent the deformed grains. The black and red lines indicate grain boundaries with misorientations above 15 deg and $\Sigma 3$ boundaries, respectively, on the band contrast background. The macroscopic shear direction is vertical (Color figure online).

corresponding hot deformation texture showed a strength of 3.8 times random (Figure 5(b)). It was composed of the A1, A2, A1*, and A2* components located along the $\{111\}\langle uvw \rangle$ fiber as well as the B1, B2, and C components situated on the $\{hkl\}\langle 110 \rangle$ fiber in the Euler space, which is typical of fcc simple shear textures produced by crystallographic slip (Figures 5(a) and (b); Table I).[25] It is seen that the C texture component dominated the orientation distribution.

The pre-existing grain boundaries commonly exhibited serration/bulging, which is a result of the strain-induced boundary migration (SIBM) mechanism operating during hot deformation.[26] However, the serration amplitude was different for each boundary depending mostly on the boundary type. The serration amplitude of annealing twin boundaries was relatively small in comparison with the general high-angle boundaries due to the minimum energy of the former,[27,28] which lowers their mobility. There were also few newly formed fine grains located mostly in the triple junctions of the pre-existing grain boundaries (shown by the arrow in Figure 4(a)), which may be formed during

deformation (*i.e.*, dynamically, DRX) or on quenching (*i.e.*, statically, SRX).

The deformation had a strong effect on the annealing twin boundary characteristics. By a strain of 0.3, some twin boundaries already started losing their coherency and their angle/axis misorientation relationships began to deviate from the original $\Sigma 3$ twin misorientation (*i.e.*, 60 deg $\langle 111 \rangle$, Figure 4(a)). The deviations were inhomogeneously distributed along the twin boundary facets (Figure 4(a)). Some twin boundary segments have lost their coherency completely while others exhibited minimal distortions. The misorientation axis vectors displayed a tendency to deviate from the [111] direction in the standard stereographic triangle (Figure 2(c)). Furthermore, the population of boundaries with misorientation angles of about 60 deg in the misorientation histogram for high-angle boundaries significantly decreased and the corresponding maximum shifted from about 60 deg towards lower angles at a strain of 0.3 (Figure 2(c)). This is due to an interaction between extrinsic (*i.e.*, glide) dislocations and the intrinsic dislocations of a twin boundary, leading to the change
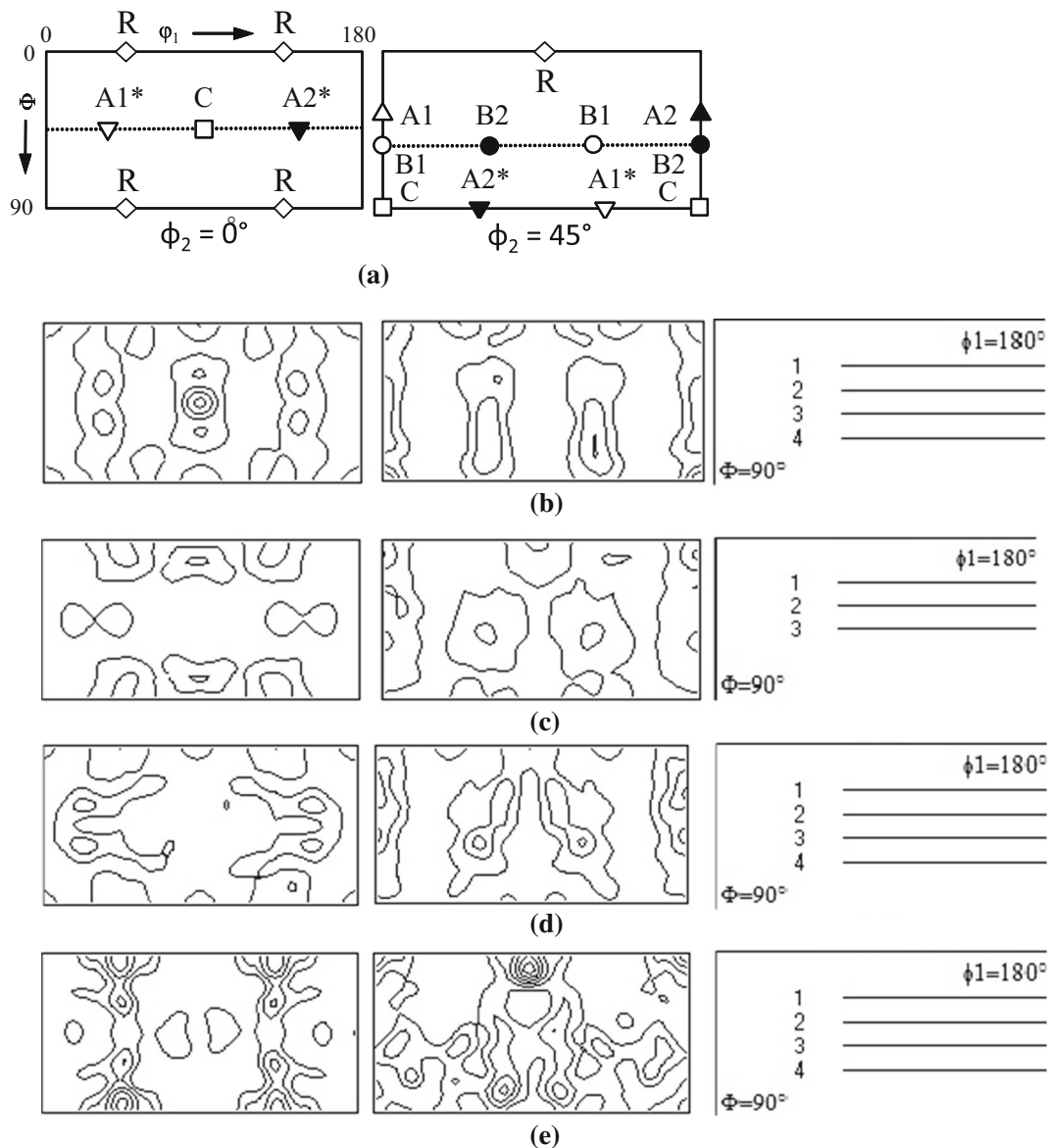
Fig. 5—(a) Ideal fcc torsion texture components in the Euler space.[25] ODF texture of the deformed matrix at 1273 K (1000 °C) with $\varepsilon = 0.3$ for different post-deformation holding times: (b) 0 s, (c) 1 s, (d) 2 s, and (e) 6 s.

in the twin interface dislocation network and thus altering the misorientation angle/axis.[29]

The TEM investigation revealed that after deformation to a strain of 0.3, the grain interiors contained well-developed regular arrays of parallel, extended MBs,[6–17] for most of the grain orientations (Figure 6). The MBs had a width of ~0.2 to 1 μm and were further subdivided along their length into shorter segments separated by low-angle boundaries. The extended longitudinal and short transverse dislocation boundaries typically exhibited misorientation angles higher than 1 deg and 0.5 to 1 deg, respectively. The MB interiors were comparatively free of dislocations, although, in some cases, an increased density of dislocations locally led to the formation of tangles and dislocation networks.

In agreement with the TEM observations, EBSD investigation showed that the grains oriented close to the main texture components A, B, and C mostly contained in their interiors families of parallel sub-boundaries delineating elongated MBs (Figure 7). The point-to-origin (cumulative) misorientation profiles measured across the band widths revealed that the band lattice orientation tended to systematically alternate across the consecutive extended sub-boundaries for all the components, which is consistent with the published literature.[12–17] The mechanism of MB formation proposed by Chen et al.[16] involves the development of parallel dislocation sheet pairs on heavily stressed crystallographic planes by cross slip. The lattice rotation is only restricted to the region between these two sheets and multiple sheets tend to form concurrently. The
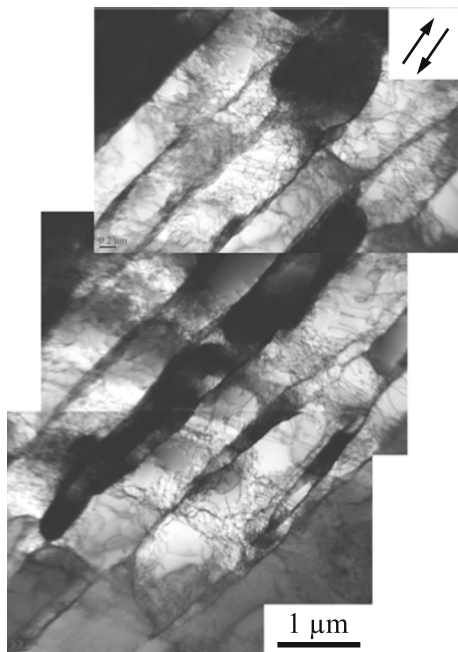
Fig. 6—TEM bright-field micrograph of the deformation substructure obtained at 1273 K (1000 °C) with $\varepsilon = 0.3$, consisting of MBs, within a grain oriented close to the A texture component. The double arrow indicates the macroscopic shear direction.

above mechanism might account for the observations of the "organized, self-screening" families of parallel MBs (Figure 7).

The substructure characteristics (*i.e.*, size and misorientation) revealed a slight change with the grain orientation. The average subgrain size (linear intercept length) was about 4.0 ± 0.8 μm for the orientation A and decreased to 3.7 ± 0.45 and 3.3 ± 0.74 μm for orientations B and C, respectively. The average misorientation angle was 0.82 ± 0.33 deg, 0.91 ± 0.46 deg, and 0.96 ± 0.7 deg for orientations A, B, and C, respectively. The change in the substructure characteristics as a function of grain orientation agrees well with the corresponding Taylor factor values; orientations A and C are associated with the lowest (*i.e.*, 1) and highest (*i.e.*, $\sqrt{3}$) Taylor factor, respectively.[30] An orientation with a higher Taylor factor (*e.g.*, C) generally requires a higher slip activity to achieve a given strain level compared to its lower Taylor factor counterpart (*e.g.*, A). As a result, it develops a higher dislocation density (*i.e.*, smaller mean subgrain size and higher misorientation) and thus higher stored energy during deformation.[30]

C. Post-Deformation Annealed State

The interrupted torsion tests clearly showed the impact of the post-deformation holding time on the behavior of the second deformation flow curves (Figure 3). At a short holding time (*e.g.*, 0.1 seconds), the second flow curve exhibited very little work hardening followed by a stress plateau. This resulted in a small softening fraction (SF) value ($\leq$10 pct, Figure 8) estimated using Eq. [1]. The second (reloading) flow curve behavior progressively changed, revealing more work hardening, with an increase in the holding time. As a result, the softening fraction progressively increased with time, the maximum softening (*i.e.*, 100 pct) being obtained at a holding time of 150 seconds (Figure 8). These changes can be directly associated with the grain structure and dislocation substructure changes taking place during the holding time.

During the post-deformation annealing, the deformed structure became gradually replaced by newly formed SRX grains (Figure 4). These grains were initially formed at the triple junctions of the pre-existing grain boundaries, where the maximum strain exists to maintain the strain compatibility between neighboring grains (Figure 4(b)). This was followed by nucleation at grain boundaries, gradually occupying most of the general boundaries (Figures 4(c) and (d)). The pre-existing $\sum$3 boundaries were mainly free of SRX grains even at the holding time of 6 seconds, where ~60 pct of the initial microstructure was replaced by these grains (Figure 4(d)). In addition, there were hardly any intragranular SRX grains observed in the deformed microstructure. Interestingly, SRX volume fraction closely matched the softening fraction estimated using the offset flow stress approach (Figure 8). The average SRX grain size was nearly constant (~18 μm) at earlier stages of recrystallization (*i.e.*, up to 10 seconds holding time) and then significantly increased with the holding time reaching ~27 μm at 150 seconds, when SRX process was completed (Figures 4(f) and 8).

Figures 5(c) through (e) show the effect of post-deformation annealing on the crystallographic texture characteristics of the deformed (recovered) matrix. It should be kept in mind that the above characteristics were significantly influenced by the way in which the matrix became consumed during the annealing process. It is seen that the pre-existing strong C texture component (see Figure 5(a)) became essentially eliminated from the orientation distribution by annealing (Figures 5(c) through (e)). Thus, this component appeared to become preferentially consumed during post-deformation annealing, in line with its comparatively high stored energy associated with the high Taylor factor. Furthermore, the orientation distribution became more complex and, interestingly, the rotated cube component R became more discernible with increasing annealing time (Figure 5). In general, the overall texture strength marginally increased from 3.8 times random at the as-deformed condition to 4.4 times random at 6 seconds holding time (Figure 5(e)), where about 60 pct of the deformed matrix was consumed through SRX (Figure 8). The crystallographic texture of SRX grains was rather weak, having a strength in a range of 2 to 2.2 times random, and maintained its character irrespective of the post-deformation holding time (Figure 9).

EBSD observations revealed that there were rather modest changes in the substructure characteristics of the deformed (recovered) matrix during the post-deformation holding (Figure 10). The presence of MBs was largely maintained in the deformed regions even when nearly 80 pct of the deformed structure became consumed by SRX grains (*i.e.*, at 20 seconds holding time,
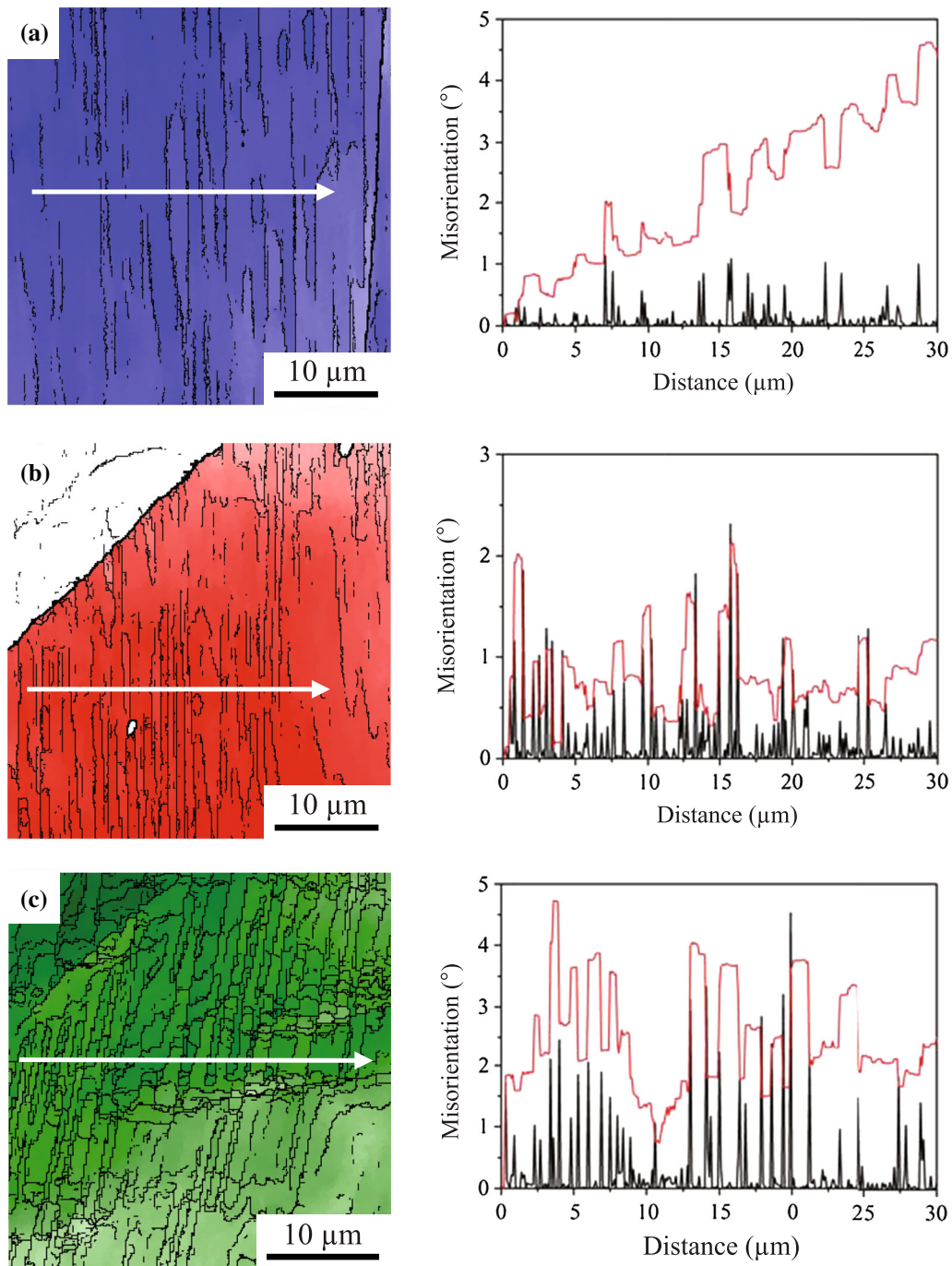
Fig. 7—EBSD maps showing the substructure developed at 1273 K (1000 °C) and $\varepsilon = 0.3$ within grains having different orientations, together with the corresponding misorientation profiles along the indicated arrows: (*a*) A, (*b*) B, and (*c*) C. The thin and thick black lines indicate boundaries with misorientations 0.5 deg $< \theta <$ 15 deg and $\theta >$ 15 deg, respectively. The background color density is inversely proportional to the deviation from the exact texture component. The macroscopic shear direction is vertical. The black and red lines in the line scan profiles represent the point-to-point and point-to-origin misorientations, respectively (Color figure online).

Figure 10(c)). The mean misorientation angle estimated for texture component A as a function of holding time remained after 2 seconds holding still equal to the starting value of about 0.82 deg, and reached values of about 0.80 deg and 0.76 deg for the holding time of 6 and 20 seconds, respectively. TEM observations further confirmed that the dislocation walls delineating MB

arrays generally maintained their integrity during post-deformation annealing, although the dislocation spacing within these walls progressively increased with increasing holding time (Figure 11), in line with the gradual reduction in misorientation angles observed by EBSD. This suggests that the extent of dislocation annihilation through the static recovery processes [1] was

not sufficient to bring about complete disintegration of the dislocation walls. In other words, the MB arrays within the deformed (recovered) matrix were mostly preserved up to the point when the latter was almost completely consumed by SRX grains. Consequently, the softening obtained during post-deformation annealing appears to have mainly originated from the

Fig. 8—Softening (SF) and recrystallized (V_{SRX}) fractions together with SRX grain size as a function of post-deformation holding time, following deformation at 1273 K (1000 °C) with $\varepsilon = 0.3$.

consumption of the deformed matrix by newly formed SRX grains, rather than from dislocation annihilation (i.e., static recovery). This conjecture is consistent with the abovementioned current observation that softening fractions on annealing, determined using the offset flow stress technique, closely matched the measured SRX volume fractions (Figure 8).

The stability of the present deformation substructure, largely consisting of MBs, on annealing appears to be markedly higher than that displayed by the random cell/subgrain substructure present within the austenite dynamically recrystallized (DRX) grains.[10] The dislocation arrangements within DRX grains of the same alloy as the one used in the present study were observed to rapidly annihilate during holding at 1273 K (1000 °C), i.e., under conditions similar to those used in the current work.[11] In fact, dislocations became almost completely removed from the DRX grain interiors after only 10 seconds of post-deformation annealing. This suggests that the nature of the dislocation substructure might govern the dislocation annihilation kinetics during annealing treatment. The organized self-screening MB arrays with mutually compensated lattice rotations appear to represent the dislocation
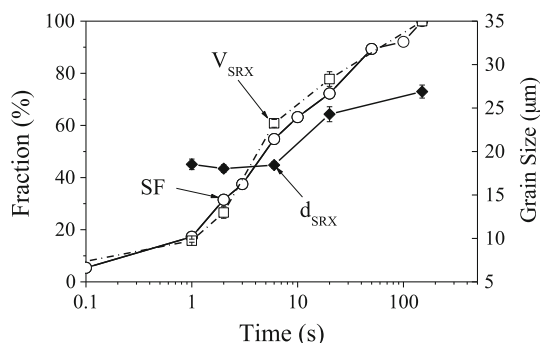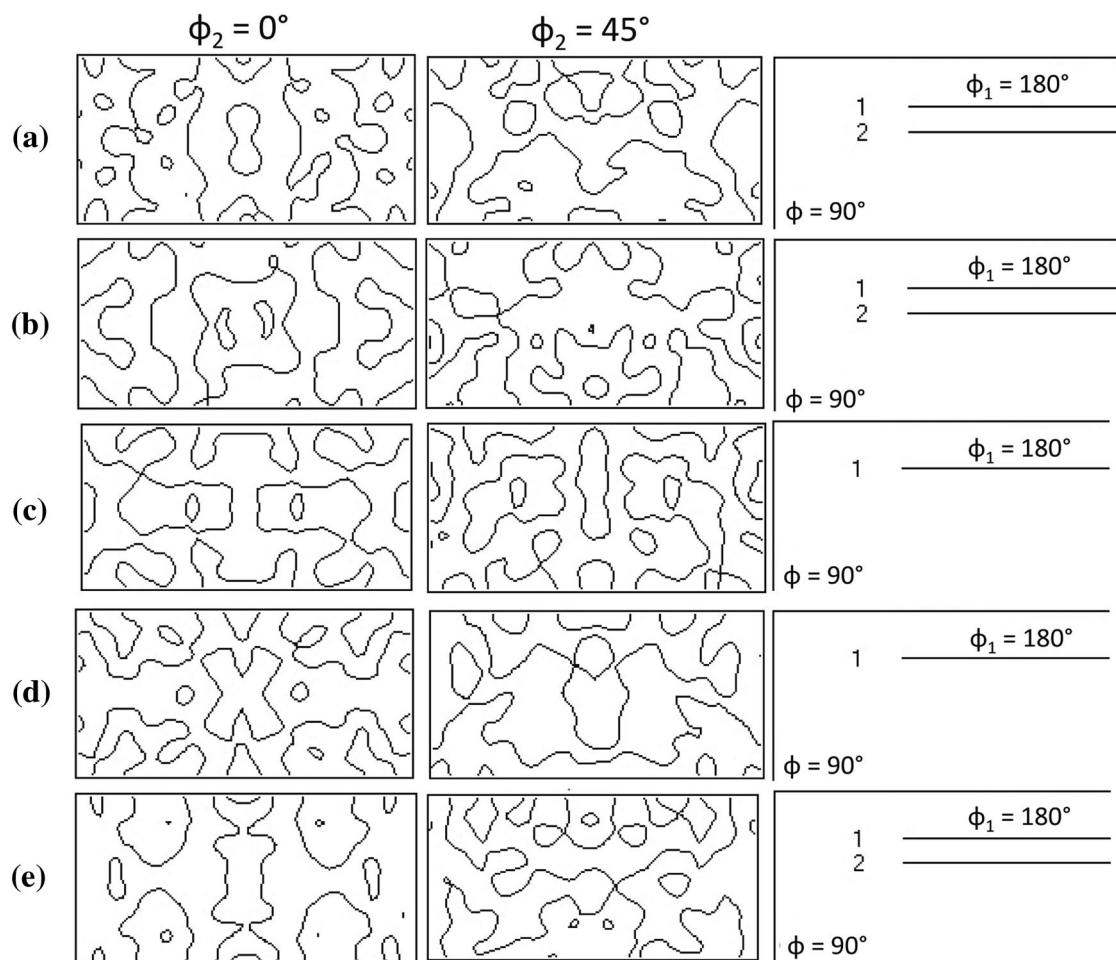

Fig. 9—ODF texture of SRX grains formed at different post-deformation holding times, following deformation at 1273 K (1000 °C) with $\varepsilon = 0.3$: (a) 1 s, (b) 2 s, (c) 6 s, (d) 20 s, and (e) 150 s.
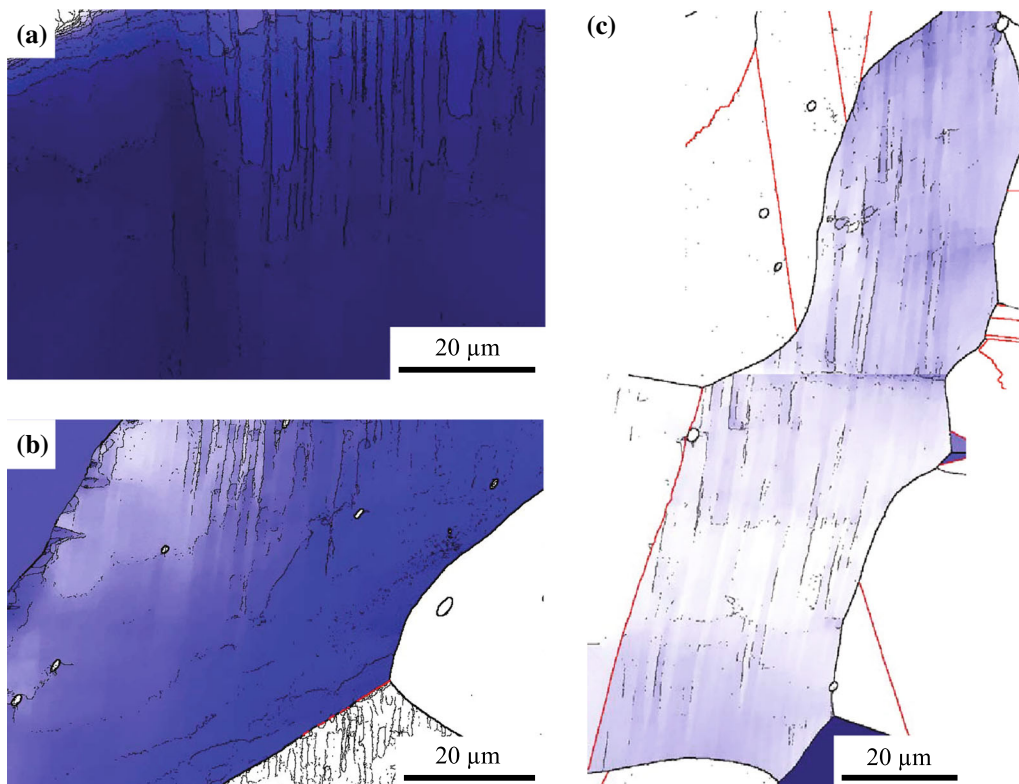
Fig. 10—EBSD maps showing the substructure of the deformed matrix grains having orientations close to the A texture component for different post-deformation holding times, following deformation at 1273 K (1000 °C) with $\varepsilon = 0.3$: (a) 2 s, (b) 6 s and (c) 20 s. The thin black, thick black, and red lines indicate boundaries with misorientations 0.5 deg $< \theta <$ 15 deg, $\theta >$ 15 deg and $\Sigma 3$ twin boundaries, respectively. The background blue color density is inversely proportional to the deviation from the exact A orientation. The macroscopic shear direction is vertical (Color figure online).
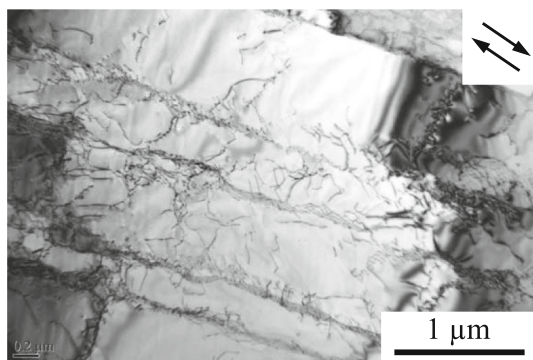

Fig. 11—TEM bright-field micrograph showing a family of MBs within a deformed (recovered) matrix grain oriented close to the A texture component, after 20-s post-deformation annealing, following deformation at 1273 K (1000 °C) with $\varepsilon = 0.3$. The MBs are bounded by planar walls consisting of dislocations that are coarsely spaced, presumably as a result of their annihilation through static recovery. The double arrow indicates the macroscopic shear direction.
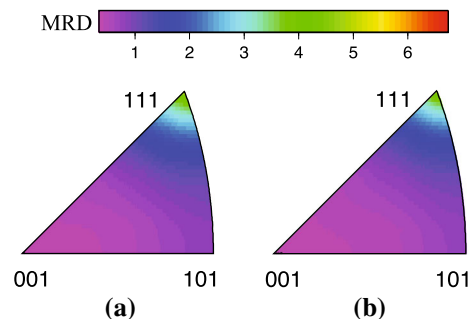

Fig. 12—The distribution of grain boundary planes ignoring misorientation angle for different SRX conditions: (a) 1273 K (1000 °C) and (b) 1473 K (1200 °C). MRD represents multiples of a random distribution.

substructure being in a markedly lower energy state (*i.e.*, closer to equilibrium) than the random cell/subgrain substructure type present within DRX grains. Therefore, it would be expected that the organized MB arrays might be considerably more stable against the dislocation annihilation, accompanying the recovery processes on annealing, compared with the random cell/subgrain substructure.

D. *SRX Grain Boundary Character Distribution*

The grain boundary character distribution was measured for both SRX conditions [*i.e.*, 1273 K (1000 °C) and 1473 K (1200 °C)] using the five-parameter crystallographic approach.[20] The distribution of grain boundary plane normals for all misorientations was plotted in the crystal reference frame, where the relative density of the normals was expressed in multiples of a random
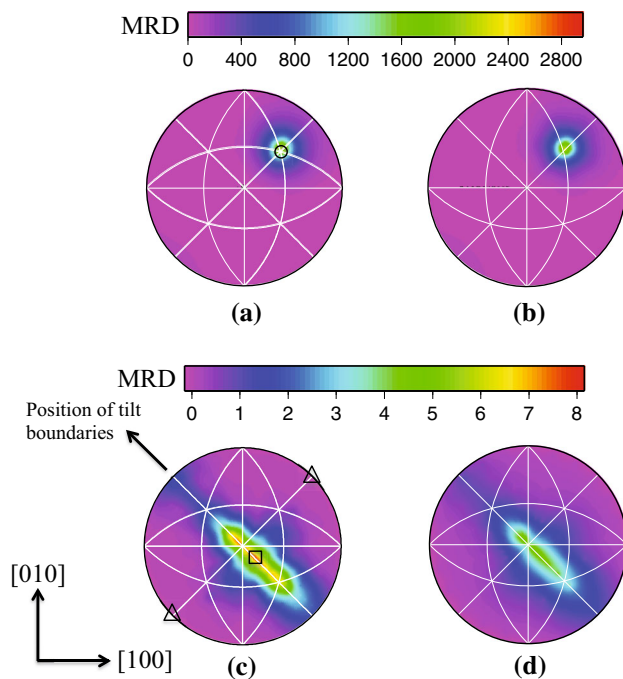
Fig. 13—The distribution of grain boundary planes at fixed misorientations of (a), (b) Σ3 = 60 deg/[111] and (c), (d) Σ9 = 38.9 deg/[110] for different static recrystallization conditions: (a), (c) 1273 K (1000 °C) and (b), (d) 1473 K (1200 °C). The circle mark in (a) represents the position of twist boundary. The triangle and square marks in (c) reveal the positions of twist and tilt boundaries, respectively. MRD is multiples of a random distribution.

distribution (MRD). The distributions revealed a strong anisotropy having a maximum at the (111) position with a value of ~6.4 and 6.72 MRD for 1273 K (1000 °C) and 1473 K (1200 °C) conditions, respectively (Figure 12). This means that the population of (111) planes was more than 500 pct higher than expected in a random distribution. By contrast, the distribution at (101) and (100) orientations was ~1 MRD and ~0.5 MRD, respectively, for both conditions. This is not surprising, as (111) planes generally represent low energy interfaces in materials with the fcc crystal structure.[27,28]

In the current study, the relative grain boundary character distribution was analyzed for certain specific CSL misorientations of Σ3 and Σ9. The distributions were drawn in the bicrystal reference frame, having the [001] direction placed perpendicular to the paper and the [100] crystal axis horizontally pointed in the plane of the paper to the right. Interestingly, the grain boundary plane distributions revealed similar characteristics for both SRX conditions. For Σ3 misorientation (*i.e.*, 60 deg/[111]), the grain boundary plane distribution showed a pronounced maximum at the (111) pure twist position with a significant population of ~2800 MRD and ~3000 MRD for 1273 K and 1473 K (1000 °C and 1200 °C), respectively (Figures 13(a) and (b)). The {111}//{111} symmetric twist grain boundary represents the coherent twin for the Σ3 misorientation in fcc materials,[27,28] having the highest grain boundary population in the distribution. By contrast, they have the lowest energy.[27,28] However, all Σ3 boundaries do not

represent coherent Σ3 boundaries, even if they fulfill Brandon's criterion.[31] In the current study, the Σ3 boundaries with grain boundary plane orientations within ±10 deg deviation of the ideal twin plane orientation were classified as coherent Σ3 boundaries. This analysis revealed that the population and length fractions of the coherent Σ3 boundaries were very similar for both conditions (Figure 14(a)). The coherent to incoherent boundary population ratio was 1.89 and 1.73 at 1273 K and 1473 K (1000 °C and 1200 °C), respectively. The coherent to incoherent length fraction ratio was 5.83 at 1273 K (1000 °C) and 6.43 at 1473 K (1200 °C) (Figure 14(b)).

Interestingly, both microstructures reveal relatively similar Σ3 boundary populations, despite distinct thermomechanical processing routes. This can be explained through the examination of factors influencing the grain boundary network, including: texture, grain morphology (formation mechanism[32,33]), processing route (temperature[27] and strain[34]), grain size[35] and composition (*i.e.* SFE[18]). Here, the composition is identical for both conditions and there are no phase changes (*e.g.*, precipitation) in the temperature range between the process temperature [1273 K and 1473 K (1000 °C and 1200 °C)] and room temperature for the Ni-30Fe alloy. In addition, both microstructures are produced through static recrystallization having equiaxed grain morphology (Figures 2(a) and 4(f)) and relatively week texture (Figures 2(b) and 9(e)).

It should be emphasized that the 1273 K (1000 °C) condition experiences an extra recrystallization cycle, *i.e.*, straining at 0.3 and holding at 1273 K (1000 °C) for 150 seconds, compared with 1473 K (1200 °C). Therefore, it would be expected that there will be greater population of Σ3 boundaries at 1273 K (1000 °C) compared with 1473 K (1200 °C), as the Σ3 boundary population increases with the number of recrystallization cycles.[36] A decrease in the grain size, *i.e.*, from ~49 μm at 1473 K (1200 °C) to ~27 μm at 1273 K (1000 °C), should also enhance the CSL boundary populations.[35] Surprisingly, this is not the case for the current result as the CSL boundary populations remain relatively similar for both thermomechanical routes.

Another difference in these processing routes is the recrystallization temperature, which influences the stacking fault energy (SFE) of material. Here, the SFE of Ni-30Fe alloy was calculated for both temperatures using an approach described in Reference 37. It appears that the SFE slightly increases with a decrease in temperature, from ~97 mJ/m^2 at 1473 K (1200 °C) to ~100 mJ/m^2 at 1273 K (1000 °C) in the Ni-30Fe alloy. The materials with lower SFE [*i.e.* 1473 K (1200 °C)] are, in general, expected to have a greater CSL boundary population than those with higher SFE [*i.e.*, 1273 K (1000 °C)].[36] In fact, relatively similar Σ3 boundary populations for two distinct thermomechanical processing routes appear to be a result of the trade off between different factors influencing the grain boundary network (*i.e.*, extra recrystallization cycle, grain size, and recrystallization temperature/SFE).

For Σ9 misorientation (*i.e.*, 38.9 deg/[110]), the boundaries were mostly positioned on the zone of pure
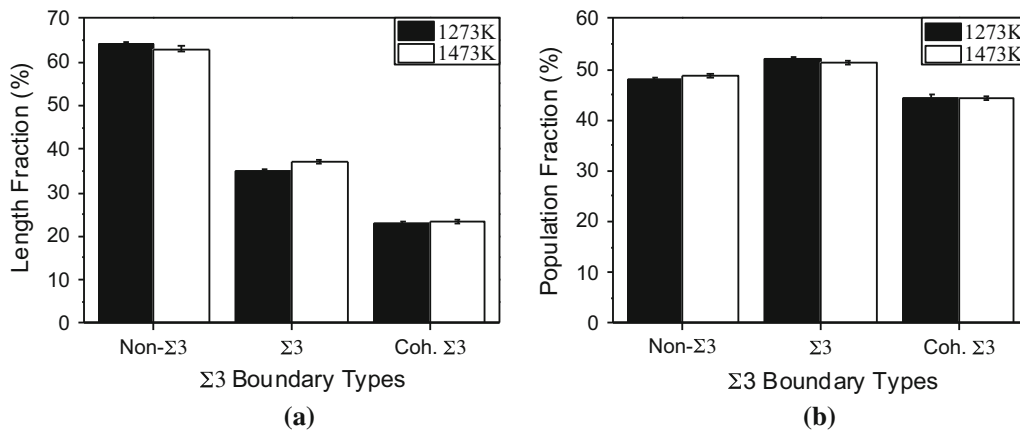
Fig. 14—The length (*a*) and population (*b*) fractions of different Σ3 boundary types for different SRX conditions. The coherent, non-coherent, and all Σ3 twin boundaries are referred to as Coh. Σ3, Non-Σ3, and Σ3, respectively.

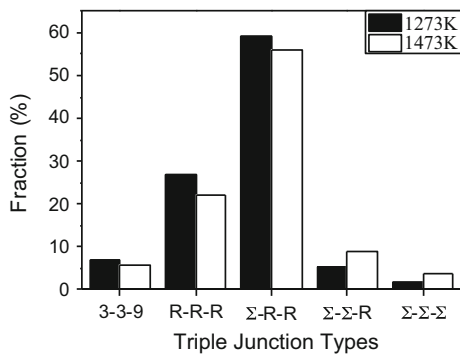

Fig. 15—The triple junction types for different SRX conditions. 3, 9, Σ, and *R* represent Σ3, Σ9, CSL boundaries, and random boundaries, respectively.

tilt boundaries having maxima mainly centered on the (1−14)//(1−14) symmetric tilt boundary for both thermomechanical routes (Figures 13(c) and (d)). However, the maximum intensity was much greater for 1273 K (1000 °C) (*i.e.*, 8.18 MRD) compared with 1473 K (1200 °C) condition (*i.e.*, 4.5 MRD). The Σ9 population is greater at the 1273 K (1000 °C) (*i.e.*, 2.5 pct) than the 1473 K (1200 °C) condition (*i.e.*, 1.6 pct). One mechanism for the formation of Σ9 is the intersection of two Σ3 boundaries (see Figure 2(a)) which do not share a common rotation axis. This is known as multiple twinning commonly observed during the microstructure evolution (*i.e.*, recrystallization and/or grain growth) of fcc materials. The Σ9 population in both conditions is consistent with the analysis of grain boundary triple junctions in both recrystallization conditions (Figure 15). The result revealed that there is a smaller fraction of triple junctions, which are made of Σ3-Σ3-Σ9, at 1473 K (1200 °C) compared with 1273 K (1000 °C). This means that the extent of multiple twinning is smaller at the 1473 K (1200 °C) than at the 1273 K (1000 °C) SRX condition, which can be related to the aforementioned factors influencing the grain boundary network evolution.

IV. CONCLUSIONS

1. Deformed grains largely contained organized self-screening arrays of MBs. The MB characteristics appeared to depend on the grain orientation, the energy stored within the MB arrays being principally consistent with the corresponding Taylor factor values.
2. The above characteristics underwent only modest changes during the post-deformation annealing. This suggests that the MB arrays had a moderate stability and the corresponding dislocation walls experienced limited dislocation annihilation.
3. SRX volume fraction closely matched the softening fraction estimated using the offset flow stress approach.
4. SRX texture was relatively weak and maintained its character independent of the holding time.
5. SRX temperature did not appear to have a significant effect on the character of CSL boundaries. The grain boundary plane distribution for Σ3 and Σ9 boundaries showed pronounced maxima for the (111) pure twist and (1−14) symmetric tilt boundary character, respectively. Nevertheless, the grain boundary network displayed a slight change with the recrystallization temperature.

REFERENCES

1. F.J. Humphreys and M. Hatherly: *Recrystallization and Related Annealing Phenomena*, 2nd ed., Elsevier Science, New York, 2004.

2. C.M. Sellars and J.A. Whiteman: *Met. Sci.*, 1979, vol. 13, pp. 187–94.
3. S.-H. Cho, K.-B. Kang, and J.J. Jonas: *ISIJ Intern.*, 2001, vol. 41, pp. 766–73.
4. H. Beladi and P.D. Hodgson: *Scripta Mater.*, 2007, vol. 56, pp. 1059–62.
5. P.J. Hurley, B.C. Muddle, and P.D. Hodgson: *Metall. Mater. Trans. A*, 2001, vol. 32A, pp. 1507–17.
6. W.M. Rainforth, M.P. Black, R.L. Higginson, E.J. Palmiere, C.M. Sellars, I. Prabst, P. Warbichler, and F. Hofer: *Acta Mater.*, 2002, vol. 50, pp. 735–47.
7. Y. Adachi, M. Wakita, H. Beladi, and P.D. Hodgson: *Acta Mater.*, 2007, vol. 55, pp. 4925–34.
8. A.S. Taylor, P. Cizek, and P.D. Hodgson: *Acta Mater.*, 2011, vol. 59, pp. 5832–44.
9. H. Beladi, P. Cizek, and P.D. Hodgson: *Metall. Mater. Trans. A*, 2009, vol. 40A, pp. 1175–89.
10. H. Beladi, P. Cizek, and P.D. Hodgson: *Acta Mater.*, 2010, vol. 58, pp. 3531–41.
11. H. Beladi, P. Cizek, and P.D. Hodgson: *Acta Mater.*, 2011, vol. 59, pp. 1482–92.
12. A.S. Taylor, P. Cizek, and P.D. Hodgson: *Acta Mater.*, 2012, vol. 60, pp. 1548–69.
13. D. Poddar, P. Cizek, H. Beladi, and P.D. Hodgson: *Metall. Mater. Trans. A*, 2015, vol. 46A, pp. 5933–51.
14. D. Poddar, P. Cizek, H. Beladi, and P.D. Hodgson: *Acta Mater.*, 2015, vol. 99, pp. 347–62.
15. Q. Liu and D. Juul: Jensen, and NHansen. *Acta Mater.*, 1998, vol. 46, pp. 5819–38.
16. Q.Z. Chen, A.H.W. Ngan, and B.J. Duggan: *Proc. R. Soc. Lond. A*, 2003, vol. 459, pp. 1661–85.
17. P. Cizek, F. Bai, E.J. Palmiere, and W.M. Rainforth: *J. Microsc.*, 2005, vol. 217, pp. 138–51.
18. V. Randle: *Acta Mater.*, 1999, vol. 47, pp. 4187–96.
19. A. Saeed-Akbari, J. Imlau, U. Prahl, and W. Bleck: *Metall. Mater. Trans. A*, 2009, vol. 40A, pp. 3076–90.
20. G.S. Rohrer, D.M. Saylor, B. El Dasher, B.L. Adams, A.D. Rollett, and P. Wynblatt: *Z. Metallkd.*, 2004, vol. 95, pp. 1–18.
21. W. Charnock and J. Nutting: *Met. Sci. J.*, 1967, vol. 1, pp. 123–27.
22. P.D. Hodgson, D.C. Collinson, and B. Perrett: *Proc. of the Int. Symp. on Physical Simulation*, NRIM, Tsukuba, 1997, pp. 219–23.
23. D.S. Fields and W.A. Backofen: *Proc. Am. Soc. Test. Mater.*, 1957, vol. 75, pp. 1259–72.
24. H.J. Bunge: *Texture Analysis in Materials Science: Mathematical Methods*, Butterworths, London, 1982.
25. L.S. Toth, P. Gilormini, and J.J. Jonas: *Acta Metall.*, 1988, vol. 36, pp. 3077–91.
26. A.M. Wusatowska-Sarnek, H. Miura, and T. Sakai: *Mater. Sci. Eng. A*, 2002, vol. 323, pp. 177–86.
27. H. Beladi, N.T. Nuhfer, and G.S. Rohrer: *Acta Mater.*, 2014, vol. 70, pp. 281–89.
28. J. Li, S.J. Dillon, and G.S. Rohrer: *Acta Mater.*, 2009, vol. 57, pp. 4304–11.
29. S. Poulat, B. Décamps, and L. Priester: *Philos. Mag. A*, 1998, vol. 77, pp. 1381–97.
30. J.J. Jonas and L.S. Toth: *Scripta Metall. Mater.*, 1992, vol. 27, pp. 1575–80.
31. D.G. Brandon: *Acta Metall.*, 1966, vol. 14, pp. 1479–84.
32. H. Beladi, G.S. Rohrer, A.D. Rollett, V. Tari, and P.D. Hodgson: *Acta Mater.*, 2014, vol. 63, pp. 86–98.
33. V. Randle, G.S. Rohrer, and Y. Hu: *Scripta Mater.*, 2008, vol. 58, pp. 183–86.
34. W. Form, G. Gindraux, and V. Mlyncar: *Met. Sci.*, 1980, vol. 14, pp. 16–20.
35. T. Watanabe, H. Fujii, H. Oikawa, and K.I. Arai: *Acta Metall.*, 1989, vol. 37, pp. 941–52.
36. G.S. Rohrer, V. Randle, C.-S. Kim, and Y. Hu: *Acta Mater.*, 2006, vol. 54, pp. 4489–4502.
37. S.L. Shang, C.L. Zacherl, H.Z. Fang, Y. Wang, Y. Du, and Z.K. Liu: *J. Phys. Cond. Matter*, 2012, vol. 24, pp. 1–14.